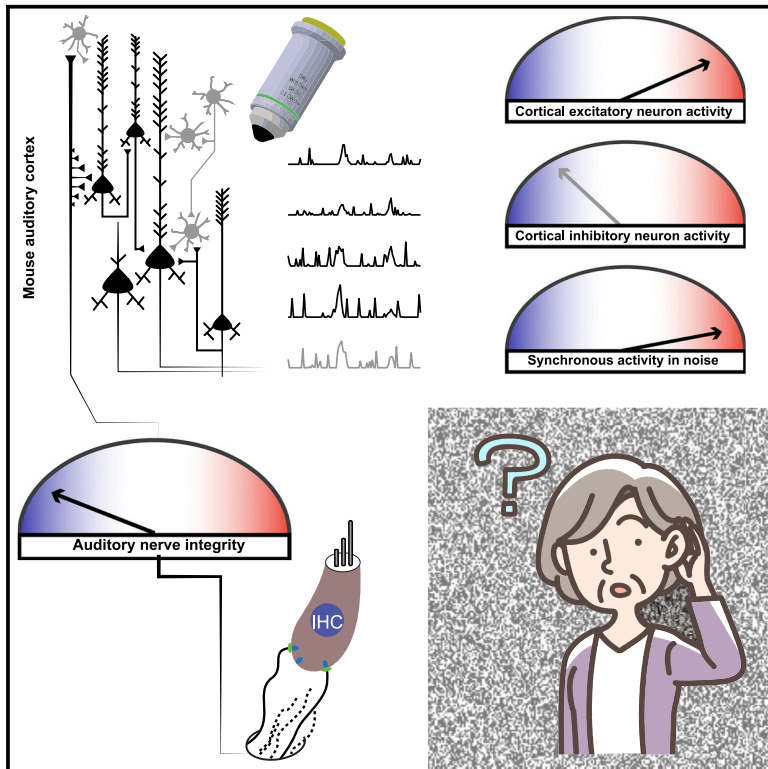# Cochlear neural degeneration disrupts hearing in background noise by increasing auditory cortex internal noise

Graphical Abstract

Authors

Jennifer Resnik, Daniel B. Polley

Correspondence

daniel_polley@meei.harvard.edu

In Brief

Resnik and Polley show that selective difficulty hearing in noise can be induced in mice through degeneration of primary afferent neurons in the auditory nerve. Primary afferent lesions dysregulate activity in the auditory cortex, producing surges of noisy, synchronized activity that specifically preceded failures to detect target sounds in noise.

Highlights

- Cochlear neural degeneration (CND) in mice causes sound detection deficits in noise

- CND induces distinct plasticity in cortical excitatory and inhibitory neurons

- Cortical hyperexcitability after CND disrupts neural adaptation to background noise

- Random surges of hypersynchronized activity precede behavioral miss trials in noise

CellPress

Neuron

CellPress

Article

Cochlear neural degeneration disrupts hearing in background noise by increasing auditory cortex internal noise

Jennifer Resnik[1,2,3] and Daniel B. Polley[1,2,4,*]
[1]Eaton-Peabody Laboratories, Massachusetts Eye and Ear Infirmary, Boston, MA 02114, USA
[2]Department of Otolaryngology—Head and Neck Surgery, Harvard Medical School, Boston, MA 02114, USA
[3]Present address: Department of Life Sciences, Ben-Gurion University of the Negev, Beersheba, Israel
[4]Lead contact
*Correspondence: daniel_polley@meei.harvard.edu
https://doi.org/10.1016/j.neuron.2021.01.015

SUMMARY

Correlational evidence in humans suggests that selective difficulties hearing in noisy, social settings may reflect premature auditory nerve degeneration. Here, we induced primary cochlear neural degeneration (CND) in adult mice and found direct behavioral evidence for selective detection deficits in background noise. To identify central determinants for this perceptual disorder, we tracked daily changes in ensembles of layer 2/3 auditory cortex parvalbumin-expressing inhibitory neurons and excitatory pyramidal neurons with chronic two-photon calcium imaging. CND induced distinct forms of plasticity in cortical excitatory and inhibitory neurons that culminated in net hyperactivity, increased neural gain, and reduced adaptation to background noise. Ensemble activity measured while mice detected targets in noise could accurately decode whether individual behavioral trials were hits or misses. After CND, random surges of hypercorrelated cortical activity occurring just before target onset reliably predicted impending detection failures, revealing a source of internal cortical noise underlying perceptual difficulties in external noise.

INTRODUCTION

Like dead pixels in a computer display, primary afferent neuropathy reduces the number of afferent transmission channels and limits the bandwidth of sensory information that can be transmitted from sensory organs to the brain. In the auditory nerve, type I spiral ganglion neurons (SGNs) transmit virtually all afferent signals from cochlear inner hair cells to postsynaptic neurons in the auditory brainstem. Type I SGNs are the most vulnerable element in the inner ear to the effects of environmental noise or aging. Work in over a dozen animal species has demonstrated a marked reduction of type I SGN synaptic contacts onto cochlear inner hair cells following exposure to ototoxic drugs, environmental noise, or just normal aging at levels that have no demonstrable effect on other cell types in the inner ear or auditory nerve (Liberman and Kujawa, 2017). In humans, post-mortem analysis of the inner ear shows that approximately 40% of SGN peripheral axons have already degenerated by age 50, well in advance of commensurate losses in other inner ear cell types (Wu et al., 2019).

Even a small fraction of functional pixels would be sufficient to determine whether a computer was on or off. The difficulty would come in the recognition of more complex images. Likewise, eliminating as much as 95% of type I SGNs in mice has minimal effects on behavioral detection in quiet backgrounds (Chambers et al., 2016a). Instead, perceptual deficits stemming from selective type I SGN degeneration are expected to occur in the presence of background noise, where redundant coding across afferent nerve fibers is critical for encoding sounds with low signal-to-noise ratios (Lopez-Poveda, 2014; Monaghan et al., 2020; Zeng et al., 2005). Prior efforts to model behavioral detection deficits in noise with pure cochlear afferent lesions in animal models have met with mixed results; in one case, a selective hearing in noise deficit was found (Lobarinas et al., 2016), and in another no association was observed (Henry and Abrams, 2021). In humans, the peripheral etiology underlying selective deficits in speech in noise can be inferred, but not proven, and the relationship to auditory nerve degeneration also remains controversial (Bharadwaj et al., 2019; Bramhall et al., 2019; Carney, 2018; Grant et al., 2020; Parthasarathy et al., 2020; Zeng et al., 2005).

From a peripheral perspective, degraded encoding of the target sound would be the primary cause for poor detection in noise following cochlear neural degeneration (CND). But an alternative possibility is that CND interferes with downstream processes in the brain that support adaptation to background noise (Bakay et al., 2018). Auditory cortex (ACtx) neurons rapidly adapt to background noise statistics to support robust, noise-invariant encoding of foreground target sounds (Atiani et al., 2009;

Rabinowitz et al., 2013; Robinson et al., 2016; Willmore et al., 2014). Although the synaptic and local circuit mechanisms have yet to be fully resolved, the evidence suggests that ACtx neurons adapt to ongoing noise statistics through rapid adjustments of intracortical inhibition and short-term dynamics of excitatory synapses (Christensen et al., 2019; Cooke et al., 2020; McGinley et al., 2015; Mesgarani et al., 2014; Natan et al., 2015; Phillips et al., 2017). Intriguingly, many of the same cortical processes involved in adaptation to background noise are also substantially altered as part of the cortical compensatory plasticity response to auditory deprivation in adult animals. A combination of increased mRNA levels for AMPA-receptor subunits and reduced transcription levels for $GABA_A$-receptor subunits (Balaram et al., 2019) reduced feedforward inhibition onto pyramidal neurons (Resnik and Polley, 2017; Yang et al., 2011) and increased intrinsic excitability (Yang et al., 2012), and upward scaling of AMPA-receptor synaptic currents (Teichert et al., 2017) effectively produce an overamplified ACtx that can compensate faster and more completely than subcortical stations for even extreme losses of cochlear afferent input (Auerbach et al., 2019; Chambers et al., 2016a, 2016b; Qiu et al., 2000). This raises the possibility that the underlying circuit changes underlying increased neural gain in ACtx support the restoration of sound processing and perception in quiet backgrounds but may actively interfere with cortical circuit mechanisms that normally support adaptation to background noise.

Here, we addressed the connection between specific hearing in noise deficits and auditory nerve damage in a mouse model of selective type I SGN loss. We adapted an approach for chronic two-photon calcium imaging so that we could simultaneously measure ensembles of individual parvalbumin-expressing (PV) GABAergic neurons and pyramidal neurons over many weeks, at single-day resolution. This approach allowed us to use each cell as its own control to assess the effects of CND on excitatory and inhibitory plasticity under passive listening conditions but also to relate ensemble dynamics to the success or failure to perceive sounds in background noise during concurrent behavioral testing.

RESULTS

CND impairs behavioral detection of tones in noise but not in silence

In mice, cochlear round window application of ouabain—a Na^+K ATP-ase inhibitor—selectively eliminates type I SGNs throughout the cochlear frequency map without affecting other neural or sensory cells in the inner ear (Yuan et al., 2014). We applied ouabain or vehicle solution bilaterally at the cochlear round window to reduce the number of synaptic contacts onto inner hair cells and to attenuate the amplitude of wave 1 of the auditory brainstem response (ABR), which is generated by synchronized type I SGN action potentials (Melcher et al., 1996; Figures 1A and 1B). Two weeks after bilateral ouabain application, we observed that ABR wave 1 amplitude at 70-dB sound pressure level (SPL) was reduced by nearly 70% (Figure 1C, statistical reporting provided in figure legends), and ABR thresholds were elevated by approximately 30 dB at all test frequencies (Figure 1D). Measurements of distortion product otoacoustic emission thresholds from the same ears were unaffected, confirming that the ouabain pro-

tocol used here induced a moderate CND in both ears without affecting pre-neural sensory transduction (Figure 1E).

To test the hypothesis that partial CND would selectively impair behavioral detection of sounds in noise, we tested the same mice in a Go/NoGo operant detection task before and after bilateral ouabain or vehicle application (Figure 1F). Well-defined psychometric tone detection functions with low false alarm rates were obtained from head-fixed mice under all conditions, although it was clear that detection thresholds in the presence of background noise were impaired after CND (Figures 1G, S1A, and S1B). We observed the same pattern for every mouse in our test sample (N = 10/10 CND/control): behavioral detection thresholds for tones in quiet were unaffected by CND, even though ABR thresholds in the same mice were substantially elevated (Figure 1H, left). In contrast, detection thresholds in the presence of 50-dB SPL white noise were elevated by approximately 15 dB in mice with CND compared with either with their baseline performance or with mice treated with a vehicle control solution (Figure 1H, right). Impaired detection of tones in noise after CND was more pronounced at low signal-to-noise ratios and for shorter tone durations, as predicted from computational models of sound encoding in the auditory nerve (Figures S1C–S1F; Lopez-Poveda, 2014).

Separate trajectories for ACtx excitatory and inhibitory neural changes produce net cortical hyperactivity

Why were tone response thresholds elevated in quiet for the ABR but not behavior? The typical explanation is that simple behavioral tasks such as detecting tones in quiet require only a small fraction of surviving peripheral afferents. Although evidently true, this explanation fails to highlight an active role for increased neural gain in the ACtx that effectively amplifies cortical sound processing downstream of the subcortical ABR generators (Chambers et al., 2016a). In the adult ACtx, homeostatic plasticity processes in excitatory pyramidal neurons reflect a combination of increased intrinsic excitability, disinhibition by downregulation of postsynaptic GABA receptors, and sensitization by upregulation of postsynaptic AMPA receptors and AMPA-mediated synaptic currents (Asokan et al., 2018; Balaram et al., 2019; Resnik and Polley, 2017; Teichert et al., 2017; Yang et al., 2011, 2012). Changes in ACtx inhibitory neurons have well-defined roles in experience-dependent development and adult learning but have never been directly studied in the context of central gain regulation in adult peripheral injury models (Abs et al., 2018; D'amour and Froemke, 2015; Kuchibhotla et al., 2017; Letzkus et al., 2011; Sarro et al., 2015; Takesian et al., 2012, 2018). PV neurons are a clear candidate for targeted recordings because they target the perisomatic compartment to throttle the excitability of postsynaptic pyramidal neurons, but also because PV-mediated feedforward inhibition is markedly reduced immediately following CND and does not return to baseline levels over several weeks of testing (Resnik and Polley, 2017). Reduced feedforward inhibition from PV neurons almost certainly reflects changes in postsynaptic GABA receptors on pyramidal neurons, but pyramidal neuron hyperactivity following cochlear afferent loss could also reflect a sustained reduction of presynaptic PV activity rates (Figure 2A).

To simultaneously and independently track changes in PV and putative pyramidal neurons (PPys), we performed daily chronic
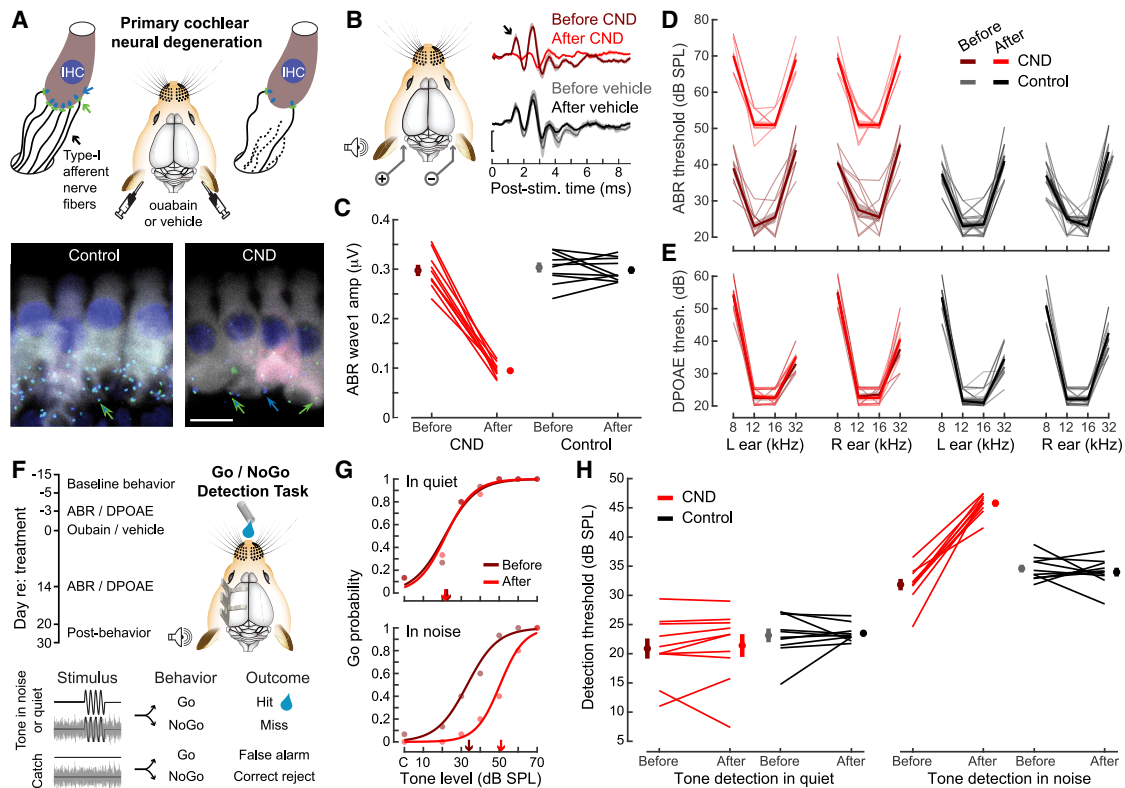
Neuron
Article

CellPress

Figure 1. Primary afferent CND disrupts behavioral detection of tones in noise but not in silence

(A) Top: schematic depicting an approach for partial elimination of auditory nerve fiber afferent synapses onto inner hair cells (IHCs) with bilateral application of ouabain to the cochlear round window. Blue arrow, IHC presynaptic ribbons; green arrow, glutamatergic postsynaptic receptors on Type-I SGN nerve terminals. Bottom: immunolabeling of presynaptic ribbons and postsynaptic terminals from the cochleas of CND and vehicle control mice. Appositions of ribbons and receptors identify afferent synapses (multi-colored arrows), whereas orphaned receptors or ribbons are identified by single-color arrows. Scale bar, 10 μm.

(B) Schematic for ABR measurements. Mean ± SEM. ABR waveforms elicited by a 12-kHz tone at 70-dB SPL. Arrow denotes wave 1. Scale bar, 0.5 μV.

(C) ABR wave 1 amplitude before and 2 weeks after ouabain (left) or vehicle (right). Each line represents the mean of the left and right ears from an individual mouse elicited by 12-kHz tones at 70-dB SPL (N = 10 ouabain-treated and 10 control mice). Symbols to either side of the lines represent sample means ± SEM. Mixed design ANOVA, group × time interaction, F = 155.3, p = 3 × 10^{-10}.

(D and E) ABR (D) and distortion product otoacoustic emission (DPOAE) thresholds (E) at four frequencies measured from the left and right ears before and after treatment with ouabain (N = 10 mice/20 ears) or vehicle (N = 10 mice/20 ears). Thin and thick lines denote individual ears and sample mean, respectively. Thresholds are significantly increased following ouabain but not vehicle (mixed design ANOVA, group × time interaction, F = 1127.8, p = 9 × 10^{-27}) but does not vary by frequency (group × time × frequency, F = 1.62, p = 0.19). DPOAE thresholds were not affected by CND (group × time interaction, F = 0.05, p = 0.11).

(F) Timeline for scheduling behavior and cochlear function tests relative to ouabain or vehicle treatment. Schematic depicts the design of head-fixed Go/NoGo detection of a 12-kHz tone presented in interleaved blocks of silence or 50-dB SPL background noise.

(G) Psychometric detection functions from a representative mouse before and after CND. Test levels (circles) are fit using binary logistic regression (lines). Downward arrows, detection thresholds; C, catch trials.

(H) Behavioral detection thresholds from the same cohort of CND and control mice characterized above. Plotting conventions match (C) Detection thresholds are significantly elevated following ouabain application but only in the presence of background noise (mixed design ANOVA, group × time × test condition, F = 36.26, p = 0.00001).

See also Figure S1.

two-photon imaging from the primary ACtx (A1) of awake, head-fixed mice that expressed tdTomato in PV neurons and GCaMP6s non-selectively in L2/3 neurons (Figure 2B). Expressing the stable tdTomato fluorophore in PV neurons facilitated motion correction and chronic tracking of individual neurons over several weeks but also allowed us to analyze GCaMP signals coming from PV neurons separately from surrounding PPys (Figure 2C). Using each cell as its own control, we calculated the daily change in spontaneous activity rate from the deconvolved calcium trace throughout a 2-week period following CND (N = 10 mice, n =

1,096/77 for PPy/PV) or control treatment (N = 9 mice, n = 936/69). As expected, spontaneous activity rates increased after CND in PPys but were relatively stable both in PV and PPys after vehicle treatment. We found that PV cell activity was markedly changed by CND but not at all like our simple cartoon model suggested (Figure 2A). Instead, PV activity rates were strongly elevated for approximately 1 week following CND, before returning to baseline levels by the end of the 2-week imaging period (Figures 2D and 2E). We confirmed that spontaneous activity changes were not a byproduct of only quantifying the subset of
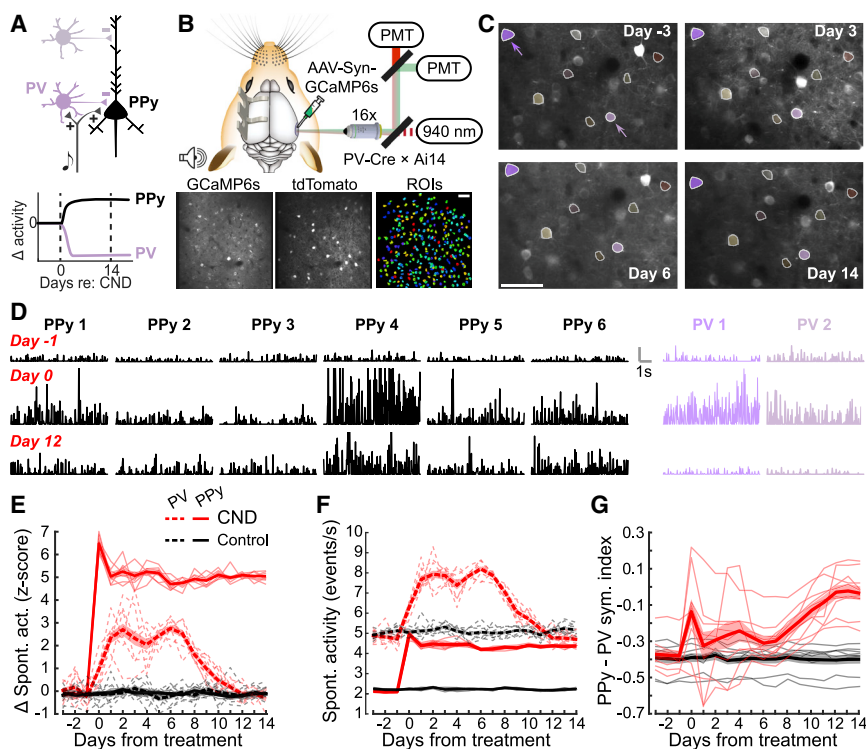
Figure 2. Different trajectories of spontaneous activity changes in PV and PPys result in net hyperexcitability

(A) Top: cartoon model of feedforward excitation from the auditory thalamus recruiting di-synaptic inhibition of cortical PPy neurons by local PV neurons. Bottom: a presynaptic basis for cortical hyperactivity could arise from sustained down-regulation of PV cell firing rates.

(B) Top: schematic of two-photon imaging in transgenic mice that express tdTomato in PV cells and virus-mediated expression of GCaMP6s in upper layer A1 neurons. Bottom (from left to right): fluorescence from the PMT tuned to shorter wavelengths (GCaMP), fluorescence from the PMT tuned to longer wavelengths (tdTomato), and semi-automated curation of all neuronal somata within the imaging field.

(C) Example of chronic tracking of individual PPys (multicolor) and PV neurons (purple shading and arrows) over 18 days of imaging (day −3 to day 14 post-treatment). Scale bar, 50 μm.

(D) Deconvolved spontaneous activity traces over an 8-s period are shown for 6 PPy and 2 PV neurons at three time points: 1 day prior to CND, the day of CND, and 12 days following CND. Vertical scale bar denotes 50 events per second and applies to all plots.

(E) Change in spontaneous activity rates for chronically tracked cells expressed a Z score relative to the distribution of spontaneous activity rates recorded over the 3-day baseline period. N = 10 CND and 9 control mice; n = 1,096/77 and 936/69 chronically tracked PPy/PV neurons in CND and control mice, respectively. Thin lines denote individual mice. Thick lines and shading denote mean ± SEM. Activity rates are increased over time following CND compared with those of control (mixed design ANOVA, group × time interaction, F = 39.23, p = 5 × 10^{-74}), but the time course of change is significantly different in PV neurons compared with that of PPys (group × time × cell type interaction, F = 18.75, p = 2 × 10^{-33}).

(F) Spontaneous activity rate measures of all PPy and PV cells unreferenced to a temporal baseline; n = 32,373/3078 and 28,323/2852 PPy/PV neurons in CND and control mice, respectively. Thin lines denote individual mice. Thick lines and shading denote mean ± SEM. Activity rates are significantly changed over time after CND compared with control, but PPy and PV exhibit significantly different trajectories of change (mixed design ANOVA, group × time × cell type interaction, F = 237.49, p = 2 × 10^{-53}).

(G) The excitatory/inhibitory balance is defined from the mean activity rate of all PPy and PV cells in the imaging field on each day per mouse with an asymmetry index ((PPy − PV) / (PPy + PV)). Negative and positive values denote higher net activity rates in PV or PPy neurons, respectively. Thin lines denote individual mice. Thick lines and shading denote mean ± SEM. Mixed design ANOVA, group × time interaction, F = 11.6, p = 0.00006.

stable cells that could be tracked across the 2- to 3-week imaging period by quantifying all PPy and PV neurons in the imaging field without referencing their activity to baseline imaging sessions (n = 32,373/3,078, PPy/PV) and vehicle controls (n = 28,323/2,852). Apart from confirming electrophysiological observations that PV cell firing rates are higher overall than PPys, we observed the same independent trajectories of PV and PPy activity rates, as seen in chronically tracked cells (Figure 2F). Additionally, because PV firing rates returned to baseline while PPys remained elevated, the asymmetry index of PV-PPy firing rate calculated from the average of all PV or PPyNs in the imaging field increasingly shifted toward net hyperexcitability following CND (Figure 2G).

Sound-evoked responses recover more completely in PPys than PV neurons, but only under quiet background conditions

To address whether behavioral recovery of detection thresholds for tones under quiet versus noisy background conditions could be attributed to the differential recovery of A1 processing, we measured sound-evoked responses in passively listening mice by using the same stimulus parameters as the behavior experiments. An example PPy exhibited a near-complete loss of sound-evoked activity on the day of CND but rebounded 12 days later, such that the gain (i.e., growth in sound response per unit step in sound intensity) was elevated above control levels (Figures 3A and S2). Less recovery in sound-evoked responses was observed in the same PPy neuron when tested in the presence of continuous noise (Figure 3B). An example PV neuron showed a similar elimination of sound-evoked activity on the day of CND, but a relatively limited recovery of evoked responses in quiet (Figure 3C) or background noise (Figure 3D).

After CND, the dichotomy between detection in quiet versus noise was particularly striking at moderate sound intensities (Figure S1C). At 50-dB SPL, the behavioral sensitivity index d-prime was significantly reduced in background noise but was unaffected in silence or by vehicle control treatment (Figure 3E). Quantification of tone-evoked responses (i.e., the change in activity in the post-stimulus period relative to the pre-stimulus baseline rate) from chronically tracked cells illustrated a clear neural parallel to the behavioral findings. Tone-evoked responses at 50-dB SPL in a
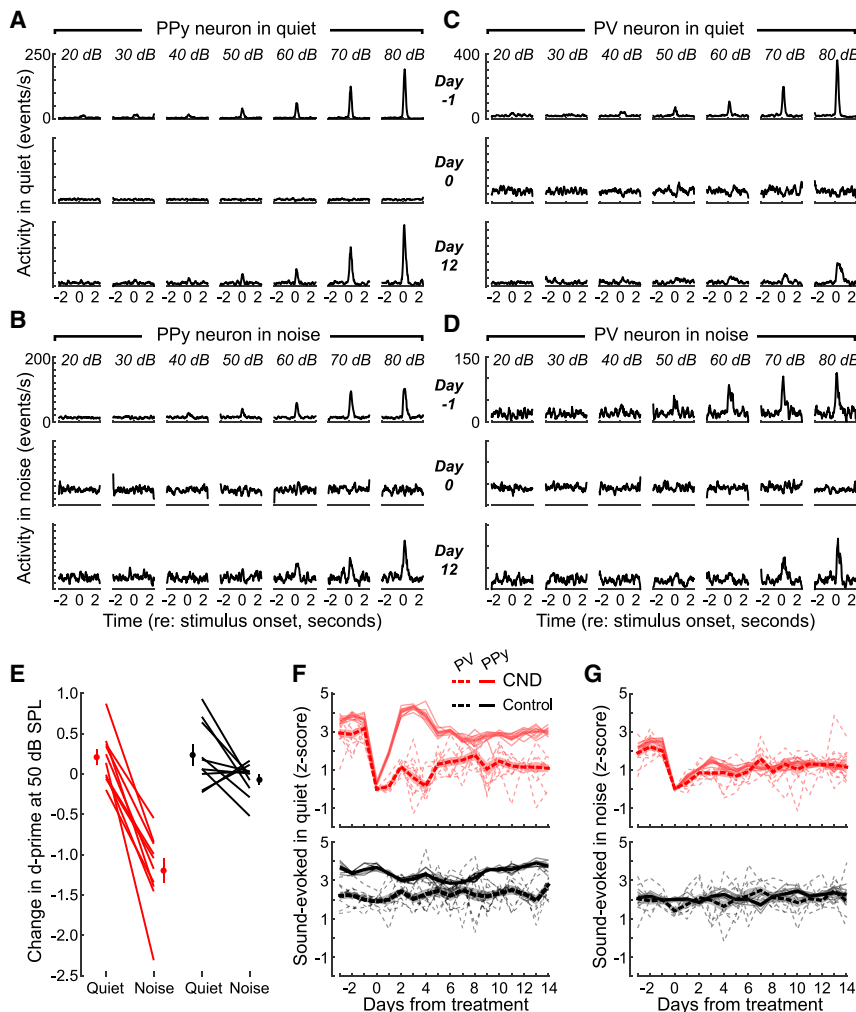
Figure 3. A near-complete recovery of sound-evoked PPy responses in silence but not in noise, whereas PV neurons show limited recovery of sound-evoked activity following CND

(A) Peri-stimulus time histograms present mean deconvolved activity rates for an example PPy on three separate measurements sessions under a quiet (top) or continuous noise (bottom) conditions. Onset of a 50-ms 12-kHz tone at intensities ranging from 20- to 80-dB SPL occurs at time = 0. y axis scaling applies to all plots.

(B) Same as (A) but in the presence of continuous background noise.

(C and D) Same as (A) and (B) but for an example PV neuron.

(E) Change in behavioral d-prime (post − pre) for a 12-kHz 50-dB SPL tone in a quiet or in the presence of 50-dB SPL broadband noise. N = 10/10 CND/vehicle control mice. Mixed design ANOVA, group × time interaction, F = 25.87, p = 8×10^{-5}).

(F) Top: sound-evoked response at 50-dB SPL in chronically tracked PPys (n = 611) and PV neurons (n = 29) in quiet from 10 mice. For each neuron, the tone-evoked activity is Z scored relative to the pre-stimulus spontaneous activity on corresponding trial. Thin lines denote individual mice. Thick lines and shading denote mean ± SEM. PPy sound responses recover more after CND than PV neurons (mixed design ANOVA, time × cell type interaction, F = 12.49, p = 3×10^{-27}). Bottom: same as above, but from n = 458 PPys and 24 PV neurons in 9 vehicle-treated control mice that show stable sound-evoked activity over time (mixed design ANOVA, main effect for time, F = 1.5, p = 0.1).

(G) Mean sound-evoked response amplitude from the same chronically tracked neurons in (F) are analyzed separately for trials in background noise. Top: sound-evoked responses in noise are reduced after CND for both PPy and PV cell types

(mixed design ANOVA, main effect for time, F = 19.43, p = 9×10^{-44}; time × cell type interaction, F = 1.1, p = 0.35). Bottom: responses are stable over time in vehicle-treated controls (mixed design ANOVA, main effect for time, F = 0.98, p = 0.46).

See also Figure S2 for changes in neural response gain and Figure S3 for changes in tone-evoked response amplitudes expressed in units of fractional change rather than deconvolved activity.

quiet background were markedly reduced on the day of CND but then recovered to near-baseline levels within a few days in PPys (n = 611). Chronically tracked PV neurons showed far less recovery throughout the 2-week recording period (n = 29), creating an imbalanced state of excitation and inhibition relative to the near equivalence of PPy and PV responses prior to CND (Figure 3F). However, when the same cells were tested in the presence of background noise, sound-evoked responses remained substantially reduced for both PPy and PV cell types (n = 458/24; Figure 3G). Our analyses focus on quantification of deconvolved GCaMP activity rates, but analysis of the fractional change in GCaMP fluorescence yielded virtually identical findings (Figure S3).

PPy ensemble stimulus decoding accuracy recovers in silence but not in noise

To address whether the combination of spontaneous hyperexcitability and reduced sound-evoked responses were related to divergent behavioral outcomes in silence and noise, we simu-

lated a detection task by decoding PPy ensemble responses in passively listening mice. We used a decoder to identify the presence of a 50-dB SPL target sound based on the separability of pre- and post-stimulus activity from 25 single trials in fixed ensembles of L2/3 PPys tracked over the 2- to 3-week imaging period (N = 10/9 for CND/vehicle mice; Figure 4A). We first reduced the dimensionality of the ensemble data matrix with principal-component analysis and then used a binary support vector machine on the principal-component projection to classify whether ensemble activity came from the pre- or post-stimulus period (Figure 4B).

In a quiet background, despite the persistent elevation of spontaneous activity in the pre-stimulus period (Figure 4A), stimulus decoding accuracy was reduced by approximately 15% over the first few days following CND but then recovered to near-perfect decoding accuracy by the end of the imaging period (Figure 4C). Prior to CND, cortical ensembles adapted to the continuous noise background and reliably encoded the
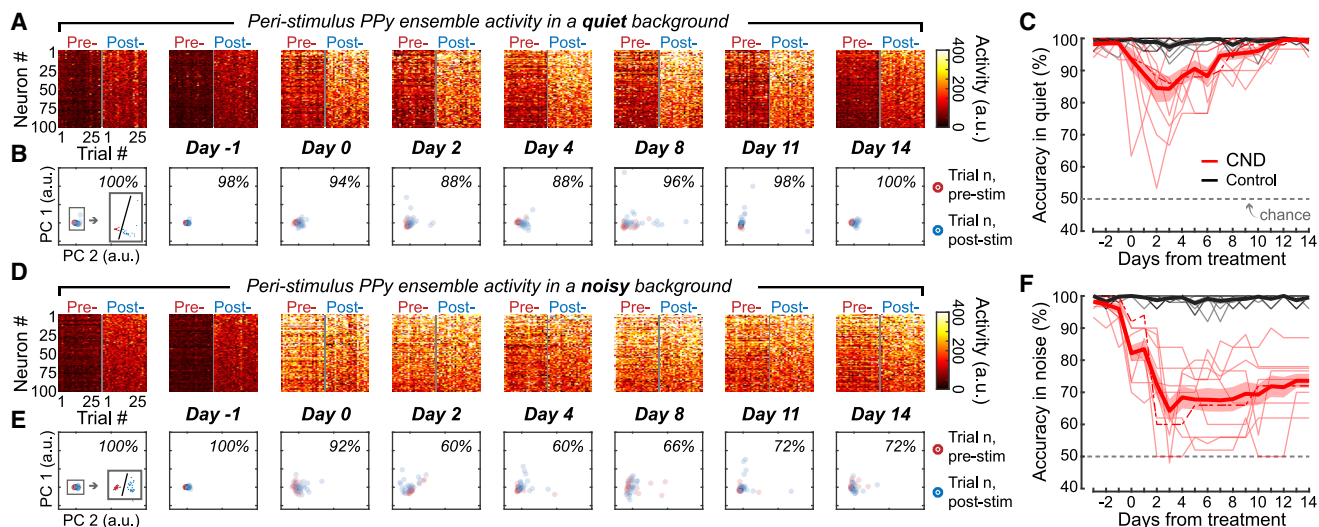
Figure 4. Single-trial stimulus decoding accuracy from PPy ensembles recovers in silence but not in noise

(A) An ensemble of the same 100 PPys from an example mouse tracked from day −3 (far left) to 14 days following CND. Each row presents the activity of a single PPy during the pre- or post-stimulus period. Each column presents the activity from 25 single-trial presentations of a 50-dB SPL target tone. Each individual data point presents the mean activity rate within a 100-ms period just before or just after stimulus onset.

(B) Pre- and post-stimulus ensemble activity from the corresponding day projected onto the first two principal components (PCs). A support vector machine was used to classify ensemble activity to pre- or post-stimulus categories. Classification accuracy is provided for each day. Inset: The pre- and post-stimulus activity period from the same 25 trials on day −3 are presented at higher magnification along with a depiction of the support vector machine hyperplane that optimally separated the two categories (black line).

(C) Stimulus classification accuracy in quiet presented for N = 10/9 CND/vehicle control mice. Thin and thick lines represent ensemble classification from an individual mouse and the sample mean ± SEM, respectively. Thin dashed line identifies the example mouse shown in (A) and (B). Classification accuracy was significantly changed after CND (mixed design ANOVA, group × time interaction, F = 4.97, p = 0.003) but was not different from control 14 days following treatment (unpaired t test, p = 0.79).

(D and E) Same plotting conventions from the same PPy ensemble as (A) and (B) but in the presence of 50-dB SPL continuous broadband noise.

(F) Same plotting conventions for the same ensembles presented in (C) but for recordings in continuous background noise. Classification accuracy was significantly reduced after CND (mixed design ANOVA, group × time interaction, F = 17.11, p = 5 × 10^{-10}) and did not recover to control levels within 14 days following treatment (unpaired t test, p = 3 × 10^{-9}).

50-dB SPL target tone (Figure 4D). Following CND, ensemble activity did not adapt but instead was strongly recruited by the background noise. Elevated activity in the pre-stimulus period was not accompanied by a commensurate elevation of stimulus-evoked response in the post-stimulus period, effectively blurring the boundary between the pre- and post-stimulus response (Figure 4E). Like behavioral detection probability in noise (Figure 3E), single trial decoding accuracy in noise declined following CND and exhibited limited recovery through the end of the imaging period (Figure 4F).

Decoding behavioral trial outcomes from L2/3 ensembles

Separate measurements of behavior and cortical dynamics suggest that increased cortical gain indiscriminately amplifies both the target stimulus and the background noise, which could explain why detection in quiet is preserved despite a greatly reduced ABR, but also why the same benefits were not observed in continuous background noise. Behavioral outcomes in the Go/NoGo task are binary; on a given trial, the mouse either detected the target sound or it did not. Although stimulus decoding from recordings made in passively listening mice provide information about changes on average, distinguishing sensory processing associated with individual subliminal or suprathreshold trials can only be made from recordings made during behavioral task performance. As a next step, we asked whether it was possible to decode behavioral trial outcomes (hit, miss, false alarm, or correct reject) from ensembles of A1 L2/3 neurons and whether this would provide insight into why detection in noise was specifically disrupted after CND.

In a subset of mice, we performed additional two-photon imaging sessions during the Go/NoGo detection task (Figure 5A). Combined imaging and behavior experiments were performed during 10-day blocks occurring 5–15 days before treatment and again 20–30 days after treatment (N = 5/5, n = 12/10.6, n = 538/516 for mice, mean number of behavioral imaging sessions, and number of chronically tracked PPys for CND/control groups, respectively; Figure 5B). Looking at an example ensemble of 30 L2/3 PPys recorded in the baseline period prior to CND, it is obvious whether a 50-dB SPL tone resulted in a hit or miss; activity was clearly increased within the first 0.1 s following tone onset in hit trials but was virtually absent in the rare instance of a miss trial (Figure 5C, left columns). Returning to the same ensemble of 30 PPys several weeks after CND, the same signature of hit and miss trials was observed under quiet background conditions, but ensemble activity both before and
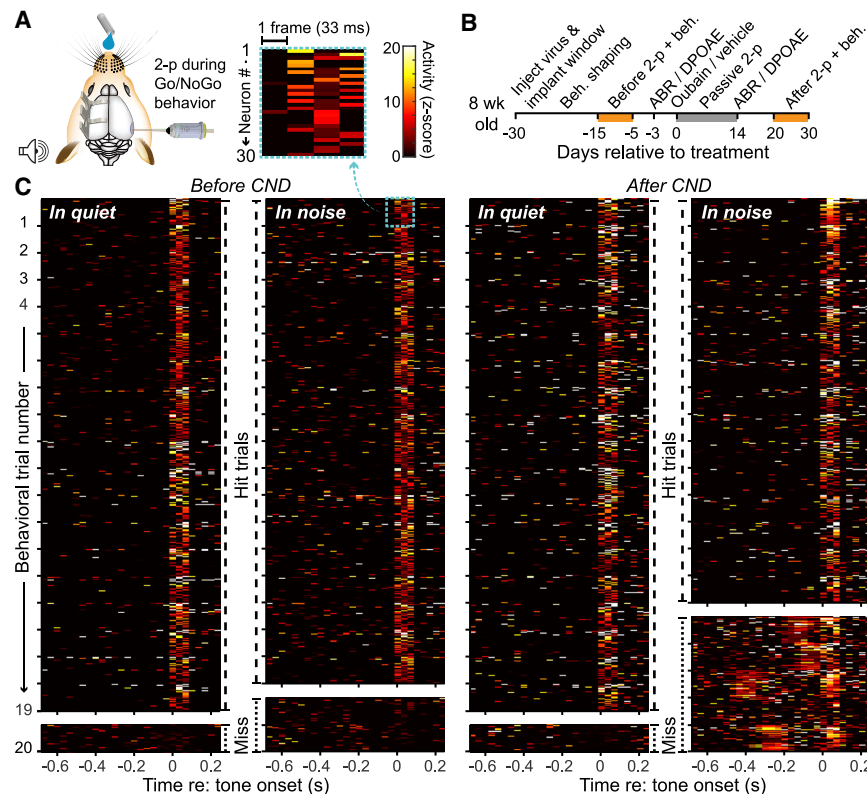
CellPress

Figure 5. Layer 2/3 ensemble dynamics during behavioral hit and miss trials
(A) Neural ensembles in L2/3 of A1 were imaged during the Go/No-Go behavioral task.
(B) Timeline of pre- and post-treatment behavioral imaging sessions relative to passive imaging and cochlear function tests.
(C) Neurograms from an example mouse present frame-by-frame activity changes for 30 PPys in 40 behavioral trials that presented a 50-dB SPL target tone in quiet background or in the presence of 50-dB SPL continuous background noise. Responses are presented separately for hit and miss trials. Activity levels were Z scored independently for each trial relative to the spontaneous activity levels during total pre-stimulus period. Color scale bar applies to all data.

tone was presented. However, we did not observe any systematic differences in L2/3 activity in false alarm trials relative to correct reject trials under any condition (Figure 6C), nor was the decoder able to classify the behavioral outcome on catch trials above chance (Figure 6D). This result confirmed our recent report that L2/3 PPγ activity is not affected by motor-related inputs

after onset of the target tone had clearly changed (Figure 5C, right columns).

We repurposed the support vector machine-based classifier (Figure 4) to decode single-trial outcomes in noise based on ensemble activity shortly following onset of the target sound. Even though differences in mean target-evoked responses are clear for hit versus miss trials under all conditions, miss trials were too rare with a 50-dB SPL tone in quiet to provide sufficient data for trial outcome classification (Figure 6A). As expected from the example case (Figure 5C) and quantification of all target-evoked responses in hit versus miss trials (Figure 6A), behavioral trial outcome in background noise was accurately decoded (>85%) from the target tone-evoked response before and after vehicle control treatment or in baseline imaging prior to CND (Figure 6B). The only exception was found in decoding trial outcomes based on the target-evoked response after CND. Although decoding accuracy remained significantly greater than chance after CND, sound-evoked responses were less distinct between hit and miss trials, leading to significantly less accurate decoding of trial outcome compared with baseline performance from the same ensembles or under control conditions.

The findings above confirm an earlier report that small ensembles of A1 L2/3 neurons can distinguish between Go and NoGo behavioral outcomes for an invariant target sound stimulus in mice with normal hearing (Francis et al., 2018). If greatly diminished sound-evoked L2/3 responses are linked to miss trials, one might also expect to see spurious elevations in L2/3 activity preceding false alarms in no-stimulus catch trials, in which mice behave as if the target

that precede licking (Clayton et al., 2020) and further suggested that behavioral false alarms either arose from exuberant activity in other cortical cell types—such as L5 sub-cerebral projection neurons (Takahashi et al., 2016, 2020)—or instead reflect a change in response bias unaccompanied by a phantom sensory percept.

Hypercorrelated activity: a source of internal noise in external noise

Looking back at the example data for activity in background noise (Figure 5C), it is evident that the distinguishing feature for hit versus miss trials in CND mice was not found in the response to the target sound but rather in the ensemble activity before the target sound.

A closer look at the pre-target activity during miss trials in noise from this example behavioral session reveals brief surges of correlated activity occurring shortly before target sound onset. This observation motivated us to ask whether hypercorrelated activity might represent a source of internal noise associated with failures to perceive target sounds in background noise. As shown in a small local network of 4 PPys and 1 PV neuron in a different example mouse, the deconvolved calcium activity traces in continuous noise were not highly correlated unless the neuropathic mouse was about to miss the target tone (Figures 7A and 7B). To quantify correlated activity, we cross-correlated the calcium traces from pairs of neurons from a 2.7-s period immediately preceding delivery of the target stimulus (Figure 7C). Plotting the mean cross correlograms confirmed that synchronized activity (i.e., increased correlation around a
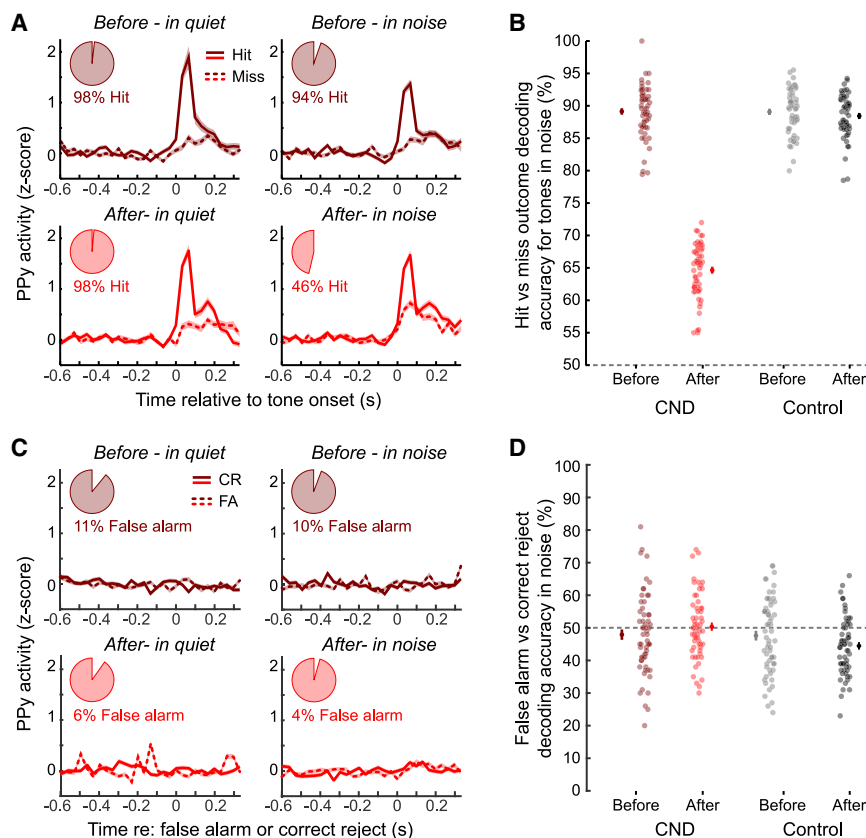
Figure 6. Decoding behavioral trial outcomes from sound-evoked L2/3 ensemble responses

(A) Mean ± SEM activity before and after CND for hit and miss trials. Single PPy activity is Z scored separately for each trial before combining across hit and miss trials in quiet/noise and before/after conditions. Pie charts present the fraction of hit trials for each condition. Data from five mice are based on 1,249/1,356 single behavioral trials before/after CND.

(B) Accuracy for support vector machine classification of behavioral trial outcome in background noise (hit versus miss) based on PPy ensemble response to the target sound. Circles represent decoding accuracy for individual behavioral sessions (60 sessions before and after CND, 53 sessions before and after vehicle). Mean ± SEM accuracy is plotted to the left and right. Classification accuracy in noise was significantly reduced after CND (mixed design ANOVA, group × time interaction, F = 643.43, p = 5 × 10^{-48}), but it is still significantly better than chance (one-sample t test against a population mean of 50%, p = 1 × 10^{-35}). Pairwise contrasts confirm that classification accuracy after CND is significantly lower than pre-CND or post-vehicle conditions after correcting for multiple comparisons (post hoc pairwise contrasts, p < 3 × 10^{-59} for both; but p = 0.93 for before versus after vehicle treatment).

(C) Plotting conventions match (A) except that data come from no-stimulus catch trials in which mice either lick the decision spout (false alarm [FA]) or withhold from licking (correct reject [CR]). Mean ± SEM. L2/3 PPy activity is plotted relative to lick onset in FA trials or relative to the average target onset time in CR trials.

(D) Accuracy for support vector machine classification of behavioral trial outcome in background noise based on PPy ensemble activity for FA and CR outcomes on no-stimulus catch trials. Plotting conventions match (B). Support vector machine classification of FA versus CR outcomes was at chance (one-sample t test against a population mean of 50%, p > 0.38 for each condition).

zero time lag) was clearly elevated prior to onset of the target stimulus for trials in which CND mice failed to detect the sound (Figure 7D).

To address whether pre-target synchrony in noise could be used to classify trial outcomes, we computed the mean positive area under the cross-correlation coefficient function (xcorr area, Figure 7C). We first tested whether increased pre-target synchrony was specific to particular cell types by separately analyzing xcorr area from hit versus miss trials in the presence of background noise in CND mice (n = 16,409 PPy-PPy pairs, n = 58 PV-PV pairs, n = 1858 PPy-PV mixed pairs). We found that synchronized activity in noise was equivalently elevated on miss trials compared with hit trials in all cell pair configurations (Figure 7E). Because the effect was consistent across cell types, we pooled all neuron pairs for the final set of analyses. We found that neural synchrony during continuous noise was significantly elevated on miss trials compared with hit trials under all conditions (before and after, CND and control; Figure 7F). However, the effect size for pre-target synchronized activity in hit versus miss trials was substantially greater after CND than that under any other condition (Hedge's g = 2.63 versus an average of 0.88). In fact, elevated synchrony after CND in miss trials was so extreme that it could be used to accurately classify whether the upcoming target stimulus would be subliminal (a miss trial)

or perceived (a hit trial). Trial outcome in noise could be decoded with 85%–90% accuracy from the response to the target sound in every condition other than CND (Figure 6B), whereas synchronized activity during the pre-target noise period could be used to classify trial outcome but only in neuropathic mice (Figure 7G). Furthermore, it was the synchrony of pre-target activity that specifically predicted trial outcome in background noise but not the overall activity rate (Figure S4).

DISCUSSION

We induced a moderate loss of type I SGNs across the cochlear frequency map by using bilateral applications of ouabain to the cochlear round window (Figures 1A–1E). We found that pure cochlear afferent lesions resulted in elevated behavioral detection thresholds in background noise without affecting threshold in quiet (Figures 1F–1H). Sound-evoked cortical PPy responses in quiet fully recovered after CND despite greatly reduced tone-evoked responses in subcortical generators of the ABR (Figures 3C and 3D). Recovered tone-evoked responses and behavioral detection in quiet were likely supported by a persistent suppression of PV neuron sound-evoked responses (Figures 3C and 4A–4C), which produced net hyperexcitability, increased central gain (Figure S2), and imbalanced spontaneous
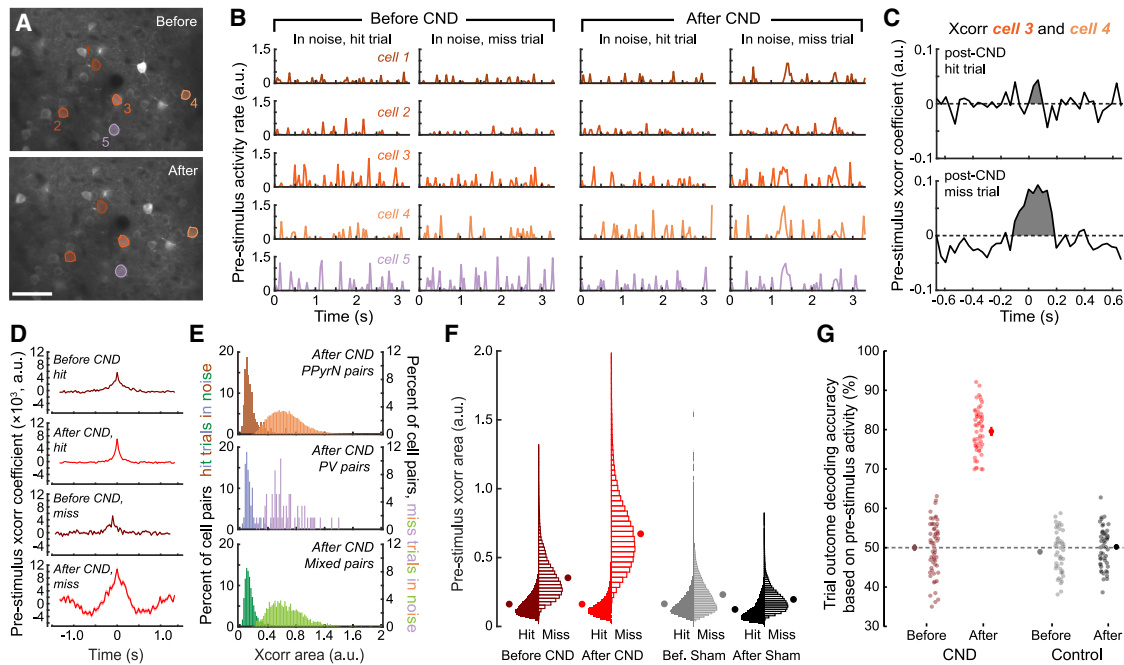
Neuron
Article

CellPress

Figure 7. Surges of synchronized activity precede failures to perceive target sounds in noise

(A) Somatic regions of interest for 4 PPys (warm colors) and 1 PV neuron (lavender). Scale bar, 50 μm.

(B) Deconvolved activity rates during continuous background noise for the five neurons in (A) over a 3.3-s period immediately prior to onset of the target sound. Recordings are shown for the same neurons during a representative hit and miss trial recorded before and after cochlear afferent CND.

(C) Mean cross-correlograms of activity traces from two PPys. Gray-shaded area denotes the positive area under the curve used to define the xcorr area.

(D) Mean ± SEM cross-correlograms before and after CND on hit versus miss trials.

(E) Histograms of xcorr area measured in noise after CND are presented for all unique combinations of PPy-PPy (n = 16,049), PV-PV (n = 58), and PPy-PV (n = 1,858) pairs tracked throughout the imaging period in hit (saturated colors, left axis) versus miss (lighter colors, right axis) trials. Note that left and right axes are scaled differently. Synchronized activity is significantly greater in miss trials than in hit trials but does not vary between cell types (mixed design ANOVA, main effect for trial outcome, F = 22,260.78, p = 0; main effect for pair type, F = 2.7, p = 0.07).

(F) Normalized histograms of xcorr area for hit and miss trials in noise are combined across all neuron pairs tracked throughout the imaging period for CND and vehicle control mice (N = 5/5 mice, n = 16,049/15,844 chronically tracked neuron pairs in CND/control groups). Data points to the side of each distribution represent the mean ± SEM of the corresponding sample. A mixed design ANOVA with a between-subjects variable (group) and two repeated measures (time and trial outcome) finds that pre-target xcorr area in noise was significantly elevated on miss trials under all four conditions (main effect for trial outcome, F = 40,156, p = 0; pairwise contrasts for Trial outcome, p < 1 × 10⁻⁶ for all). The difference in xcorr area on miss versus hit trials was greater after CND than other conditions (Hedge's g = 2.63 versus a mean of 0.88; group × time × trial outcome interaction, F = 11,716, p = 0).

(G) Accuracy for support vector machine classification of behavioral trial outcome in background noise (hit versus miss) based on synchronized activity (xcorr area) between neuron pairs prior to the onset of the target sound. Circles represent decoding accuracy for individual behavioral sessions. Mean ± SEM accuracy is plotted to the left and right. Classification accuracy is at chance before CND or before/after vehicle control (one-sample t tests against a population mean of 50%, p > 0.49 for each sample) but is significantly better than chance following CND (mixed design ANOVA, group × time interaction, F = 421.72, p = 1 × 10⁻³⁹; and one-sample t test against a population mean of 50%, p = 8 × 10⁻⁴⁴).

See also Figure S4 for control analyses based on overall activity rate and temporally shuffled activity.

activity rates in PPy and PV neurons (Figure 2). Cortical sound processing in the presence of background noise showed a different trajectory of recovery after CND, for which tone-evoked responses (Figure 3G) and single trial ensemble decoding accuracy (Figures 4D–4F) were strongly depressed and showed only minimal improvement through the end of the imaging period. In mice with normal hearing, perceptual miss trials were associated with substantially weaker responses to the target stimulus and elevated correlated activity prior to the target (Figures 6A, 6B, and 7F). After CND, surges of correlated activity in background noise were so pronounced on miss trials that we could decode trial outcome with 80% accuracy based only on neural synchrony before sound onset (Figure 7G).

Primary CND as a distal trigger—not a proximal cause—of hearing in noise deficits

The results shown here suggest a strong but indirect connection between primary CND and selective difficulties hearing in background noise. The loss of cochlear afferent channels reduces the bandwidth of sound-related signals that can be transmitted from the ear to the brain, directly depriving the auditory brainstem of the rapid spectrotemporal cues that it would normally use to segregate foreground target sounds from background noise. In addition to the loss of bottom-up information coding, CND also triggers a cascade of compensatory physiological changes that begin unfolding within the first few hours after the loss of auditory nerve input and continue to change over the following

ten days. The combination of hyperactive PPy neurons and hypoactive PV neurons compensated for moderate CND to restore sound-evoked activity in quiet, but the destabilized excitatory-inhibitory balance disrupted the normal processes that allow ACtx ensembles to adapt to continuous background noise.

The standard explanation for selective hearing in noise deficits is that perception in quiet can be preserved even with substantial degeneration of auditory nerve afferent fibers, but perception in noise requires more intact afferent nerve fibers for the brain to faithfully encode the rapid spectrotemporal co-modulations that support the separation of foreground targets from background sounds (Lopez-Poveda, 2014; Shaheen et al., 2015). Our results emphasize that it is both the direct loss of afferent coding channels in the auditory nerve and the central sequelae of hyperactivity and hypercorrelation that combine to produce the perceptual phenotype of hidden hearing loss. When humans or mice with primary CND struggle to perceive sounds at signal-to-noise ratios (SNRs) that present no challenge to neurotypical subjects, their performance deficits—as with any liminal stimulus—are fluctuant; sometimes they hear it and other times they do not. Describing the psychophysical data only in terms of the mean central tendency fails to capture the fluctuant nature of the disorder and can perpetuate the misconception that a constant and stable loss of auditory nerve fibers can account for a constant and stable failure to perceive sounds at moderate SNRs. Because the perceptual outcome is fluctuant at the SNRs that most clearly distinguished CND from sham mice (Figure S1C), neural candidates for a proximal biological cause would also have to fluctuate alongside perception. Here, we found L2/3 ensemble activity in the ACtx fluctuated so closely with perceptual hits and misses in noise that we could decode the trial outcome with over 80% accuracy based either on target-evoked or correlated activity levels. Although auditory cortical activity is tightly linked—and likely enables—sound perception, the activity in the auditory nerve and early stages of sound processing are tightly coupled to the physical stimulus (Mesgarani and Chang, 2012; Petkov et al., 2007). The loss of auditory nerve afferent fibers is perhaps more appropriately conceptualized as a distal trigger, not a proximal cause, for fluctuant difficulty in perceiving a fixed SNR target sound in background noise after CND.

Perceptual misses—errors of neural omission but also neural commission

Although primary CND has also been linked to disrupted adaptation to background noise (Bakay et al., 2018), neural and perceptual deficits after CND are generally attributed to failures in how the target stimulus is encoded (Lopez-Poveda, 2014; Monaghan et al., 2020). Both in mice with normal hearing and mice with CND, we found that perceptual miss trials in noise were associated with significant elevations in correlated activity immediately preceding the target (Figure 7F). In mice with normal hearing, the best predictor of perceptual misses in noise was found in the target-evoked response (Figure 6B; Francis et al., 2018), but after CND, the strongest predictor of impending perceptual misses were found in transient surges in correlated activity (not rate, per se; Figure S4A) occurring during the background noise, prior to target sound onset (Figure 7G). Although it may be more intuitive

to conceive of perceptual misses reflecting the omission of a neural response to sound, one can also appreciate that elevating synchronized PPy activity prior to target onset would disrupt the neural contrast between pre- and post-stimulus activity (i.e., reducing the neural SNR by elevating the "N" rather than reducing the "S"). To this point, another recent study reported that optogenetically synchronizing ACtx PPy spiking just prior to target sound onset—but not during the sound-evoked response—increased the probability of perceptual misses without increasing the probability of false alarms (Carcea et al., 2017).

The yin and yang of increased central gain

Peripheral explanations for selective hearing in noise deficits conceive of a normal brain contending with an impoverished afferent input from the nerve. This perspective is insufficient, as it disregards the profound intrinsic, synaptic, circuit, and network-level pathophysiological changes that arise in the brain as a consequence of cochlear deafferentation. Collectively, these processes increase the central gain on diminished inputs arising from the auditory periphery. But, in compensating for the loss of bottom-up afferent input, central gain processes often over-shoot the mark, making central auditory neurons hypersensitive, disinhibited, hyperactive, and hypercorrelated (Eggermont, 2017). When the damage protocols are selective to the afferent pathway and do not disrupt pre-neural sound transduction, the expression of excess central gain begins earlier and is expressed more robustly overall at the level of the ACtx than at subcortical stations (Asokan et al., 2018; Balaram et al., 2019; Chambers et al., 2016a, 2016b; Qiu et al., 2000; Resnik and Polley, 2017).

Here, we found that downregulation of sound-evoked responses in PV neurons and destabilization of PV-PyrN activity rates were associated with a homeostatic correction of sound-evoked PPy activity rates in quiet backgrounds. Pushing inhibition-stabilized recurrent networks toward disinhibition may compensate for reduced bottom-up excitatory input, likely supporting the near-complete recovery reported here for sound processing and perception in a typical quiet environment. At the same time, downregulation of local inhibition can push cortical networks toward internally noisy, unstable operating points characterized by excess gain, loss of tuning precision, and hypersynchronous bursts of activity (Barrett et al., 2016; Graupner and Reyes, 2013; Levy and Reyes, 2011; Moore et al., 2018; Renart et al., 2010; Vogels et al., 2011). With reduced synaptic inhibition and upward scaling of glutamatergic synapses (Balaram et al., 2019; Teichert et al., 2017; Yang et al., 2011), the normally weak intracortical excitatory synapses that predominate in L2/3 PPy neurons could perpetuate stochastic self-activation, particularly when combined with continuous feedforward input provided by background noise.

The relatively slow time constants of the GCaMP6s signal were unable to resolve the source of correlated activity surges, but future modeling or neurophysiological studies could investigate whether hypercorrelated activity arose from brief periods of closed-loop intracortical self-activation or instead reflected an increased incidence of burst-mode firing from feedforward thalamocortical inputs, which has been reported following hearing

Neuron
Article

🔓 **CellPress**

loss protocols that produce tinnitus (Kalappa et al., 2014; Sametsky et al., 2015). As an additional caveat, although calcium transients indicated by GCaMP6s normally correspond closely to spiking activity (Chen et al., 2013), intracellular calcium itself is a key arbiter in homeostatic plasticity signaling pathways (Turrigiano, 2008). There is always the possibility that calcium homeostasis itself has been altered after CND in a manner independent of spiking. However, changes for sound processing in quiet reported here in PPγ and PV neurons after CND were also observed with protocols relying on electrophysiology and optogenetics (Chambers et al., 2016a; Resnik and Polley, 2017).

Recovering signal in the noise

A recent behavioral report found that primary CND had no effect on tone detection in noise in budgerigars (Henry and Abrams, 2021), which is at odds with the findings we present here as well as prior behavioral measurements following selective inner hair cell lesions in chinchillas (Lobarinas et al., 2016) or neural measurements after noise-induced primary afferent synaptopathy in gerbils (Monaghan et al., 2020). The bird auditory forebrain does not exhibit the compensatory plasticity seen in many mammalian species after focal peripheral lesions (Irvine et al., 2009). One explanation for their discrepant findings is that the cortical hyperactivity and hypersynchrony described here that directly contribute to impaired detection of tones in noise do not occur in species without a neocortex. Another explanation is that their behavioral measurements were made approximately 1 year after auditory nerve lesions through 4–5 months of intensive rewarded behavioral testing using near-threshold stimuli. Perceptual learning protocols like the one used in their study have earned their name because they improve perceptual thresholds for practice stimuli by promoting selective reorganization of underlying neural representations (Caras and Sanes, 2017; Polley et al., 2006; Recanzone et al., 1993). To this point, intensively training mice to better discriminate near-threshold sounds in background noise promotes improved cortical neural resistance to background masking noise (Whitton et al., 2014). Intensively training human subjects with or without hearing impairment on a similar sound-in-noise discrimination tasks imparted improved sentence intelligibility for target speakers with multiple competing speakers in the background (Whitton et al., 2014, 2017). This raises the exciting possibility that maladaptive cortical plasticity and associated perceptual disorders that are triggered by an irreversible loss of auditory nerve afferents can be at least partially mitigated by behavioral protocols that promote positive plasticity through reinforced learning.

STAR★METHODS

Detailed methods are provided in the online version of this paper and include the following:

- KEY RESOURCES TABLE
- RESOURCE AVAILABILITY
  - Lead contact
  - Materials availability
  - Data and code availability
- EXPERIMENTAL MODEL AND SUBJECT DETAILS
- METHOD DETAILS
  - Survival surgeries for awake, head-fixed experiments
  - Cochlear primary afferent neuropathy
  - Cochlear function tests
  - Cochlear histology
  - Go / NoGo operant detection task
  - Virus mediated gene-delivery
  - Two-photon calcium imaging
- QUANTIFICATION AND STATISTICAL ANALYSIS
  - Two-photon imaging analysis
  - Statistical analysis

AUTHOR CONTRIBUTIONS

D.B.P. and J.R. designed the experiments. J.R. performed all experiments and analysis with supervisory input from D.B.P. D.B.P. wrote the manuscript with input from J.R.

DECLARATION OF INTERESTS

D.B.P. is a member of the *Neuron* scientific advisory board.

REFERENCES

Abs, E., Poorthuis, R.B., Apelblat, D., Muhammad, K., Pardi, M.B., Enke, L., Kushinsky, D., Pu, D.L., Eizinger, M.F., Conzelmann, K.K., et al. (2018). Learning-related plasticity in dendrite-targeting layer 1 interneurons. Neuron *100*, 684–699.e6.

Asokan, M.M., Williamson, R.S., Hancock, K.E., and Polley, D.B. (2018). Sensory overamplification in layer 5 auditory corticofugal projection neurons following cochlear nerve synaptic damage. Nat. Commun. *9*, 2468.

Atiani, S., Elhilali, M., David, S.V., Fritz, J.B., and Shamma, S.A. (2009). Task difficulty and performance induce diverse adaptive patterns in gain and shape of primary auditory cortical receptive fields. Neuron *61*, 467–480.

Auerbach, B.D., Radziwon, K., and Salvi, R. (2019). Testing the central gain model: loudness growth correlates with central auditory gain enhancement in a rodent model of hyperacusis. Neuroscience *407*, 93–107.

Bakay, W.M.H., Anderson, L.A., Garcia-Lazaro, J.A., McAlpine, D., and Schaette, R. (2018). Hidden hearing loss selectively impairs neural adaptation to loud sound environments. Nat. Commun. *9*, 4298.

Balaram, P., Hackett, T.A., and Polley, D.B. (2019). Synergistic transcriptional changes in AMPA and GABA$_A$ receptor genes support compensatory plasticity following unilateral hearing loss. Neuroscience *407*, 108–119.

Barrett, D.G., Denève, S., and Machens, C.K. (2016). Optimal compensation for neuron loss. eLife 5, 1–36.

Bharadwaj, H.M., Mai, A.R., Simpson, J.M., Choi, I., Heinz, M.G., and Shinn-Cunningham, B.G. (2019). Non-invasive assays of cochlear synaptopathy—candidates and considerations. Neuroscience 407, 53–66.

Bramhall, N., Beach, E.F., Epp, B., Le Prell, C.G., Lopez-Poveda, E.A., Plack, C.J., Schaette, R., Verhulst, S., and Canlon, B. (2019). The search for noise-induced cochlear synaptopathy in humans: Mission impossible? Hear. Res. 377, 88–103.

Caras, M.L., and Sanes, D.H. (2017). Top-down modulation of sensory cortex gates perceptual learning. Proc. Natl. Acad. Sci. U S A 114, 9972–9977.

Carcea, I., Insanally, M.N., and Froemke, R.C. (2017). Dynamics of auditory cortical activity during behavioural engagement and auditory perception. Nat. Commun. 8, 14412.

Carney, L.H. (2018). Supra-threshold hearing and fluctuation profiles: implications for sensorineural and hidden hearing loss. J. Assoc. Res. Otolaryngol. 19, 331–352.

Chambers, A.R., Resnik, J., Yuan, Y., Whitton, J.P., Edge, A.S., Liberman, M.C., and Polley, D.B. (2016a). Central gain restores auditory processing following near-complete cochlear denervation. Neuron 89, 867–879.

Chambers, A.R., Salazar, J.J., and Polley, D.B. (2016b). Persistent thalamic sound processing despite profound cochlear denervation. Front. Neural Circuits 10, 72.

Chen, T.-W., Wardill, T.J., Sun, Y., Pulver, S.R., Renninger, S.L., Baohan, A., Schreiter, E.R., Kerr, R.A., Orger, M.B., Jayaraman, V., et al. (2013). Ultrasensitive fluorescent proteins for imaging neuronal activity. Nature 499, 295–300.

Christensen, R.K., Lindén, H., Nakamura, M., and Barkat, T.R. (2019). White noise background improves tone discrimination by suppressing cortical tuning curves. Cell Rep. 29, 2041–2053.e4.

Clayton, K.K., Williamson, R.S., Hancock, K.E., Tasaka, G.I., Mizrahi, A., Hackett, T.A., and Polley, D.B. (2020). Auditory corticothalamic neurons Are recruited by motor preparatory inputs. Curr. Biol. 31, 1–13.

Cooke, J.E., Kahn, M.C., Mann, E.O., King, A.J., Schnupp, J.W.H., and Willmore, B.D.B. (2020). Contrast gain control occurs independently of both parvalbumin-positive interneuron activity and shunting inhibition in auditory cortex. J. Neurophysiol. 123, 1536–1551.

D'amour, J.A., and Froemke, R.C. (2015). Inhibitory and excitatory spike-timing-dependent plasticity in the auditory cortex. Neuron 86, 514–528.

Eggermont, J.J. (2017). Acquired hearing loss and brain plasticity. Hear. Res. 343, 176–190.

Francis, N.A., Winkowski, D.E., Sheikhattar, A., Armengol, K., Babadi, B., and Kanold, P.O. (2018). Small networks encode decision-making in primary auditory cortex. Neuron 97, 885–897.e6.

Friedrich, J., Zhou, P., and Paninski, L. (2017). Fast online deconvolution of calcium imaging data. PLoS Comput. Biol. 13, e1005423.

Grant, K.J., Mepani, A.M., Wu, P., Hancock, K.E., Gruttola, V., De Liberman, M.C., and Maison, S.F. (2020). Electrophysiological markers of cochlear function correlate with hearing-in-noise performance among audiometrically normal. J. Neurophysiol. 124, 418–431.

Graupner, M., and Reyes, A.D. (2013). Synaptic input correlations leading to membrane potential decorrelation of spontaneous activity in cortex. J. Neurosci. 33, 15075–15085.

Henry, K.S., and Abrams, K.S. (2021). Normal tone-in-noise sensitivity in trained budgerigars despite substantial auditory-nerve injury: no evidence of hidden hearing loss. J. Neurosci. 41, 118–129.

Irvine, D.R.F., Brown, M., Kamke, M.R., and Rubel, E.W. (2009). Effects of restricted basilar papillar lesions and hair cell regeneration on auditory forebrain frequency organization in adult European starlings. J. Neurosci. 29, 6871–6882.

Kalappa, B.I., Brozoski, T.J., Turner, J.G., and Caspary, D.M. (2014). Single unit hyperactivity and bursting in the auditory thalamus of awake rats directly correlates with behavioural evidence of tinnitus. J. Physiol. 592, 5065–5078.

Kuchibhotla, K.V., Gill, J.V., Lindsay, G.W., Papadoyannis, E.S., Field, R.E., Sten, T.A.H., Miller, K.D., and Froemke, R.C. (2017). Parallel processing by cortical inhibition enables context-dependent behavior. Nat. Neurosci. 20, 62–71.

Letzkus, J.J., Wolff, S.B.E., Meyer, E.M.M., Tovote, P., Courtin, J., Herry, C., and Lüthi, A. (2011). A disinhibitory microcircuit for associative fear learning in the auditory cortex. Nature 480, 331–335.

Levy, R.B., and Reyes, A.D. (2011). Coexistence of lateral and co-tuned inhibitory configurations in cortical networks. PLoS Comput. Biol. 7, e1002161.

Liberman, M.C., and Kujawa, S.G. (2017). Cochlear synaptopathy in acquired sensorineural hearing loss: Manifestations and mechanisms. Hear. Res. 349, 138–147.

Lobarinas, E., Salvi, R., and Ding, D. (2016). Selective inner hair cell dysfunction in chinchillas impairs hearing-in-noise in the absence of outer hair cell loss. J. Assoc. Res. Otolaryngol. 17, 89–101.

Lopez-Poveda, E.A. (2014). Why do I hear but not understand? Stochastic undersampling as a model of degraded neural encoding of speech. Front. Neurosci. 8, 348.

McGinley, M.J., David, S.V., and McCormick, D.A. (2015). Cortical membrane potential signature of optimal states for sensory signal detection. Neuron 87, 179–192.

Melcher, J.R., Guinan, J.J., Jr., Knudson, I.M., and Kiang, N.Y.S. (1996). Generators of the brainstem auditory evoked potential in cat. II. Correlating lesion sites with waveform changes. Hear. Res. 93, 28–51.

Mesgarani, N., and Chang, E.F. (2012). Selective cortical representation of attended speaker in multi-talker speech perception. Nature 485, 233–236.

Mesgarani, N., David, S.V., Fritz, J.B., and Shamma, S.A. (2014). Mechanisms of noise robust representation of speech in primary auditory cortex. Proc. Natl. Acad. Sci. USA 111, 6792–6797.

Monaghan, J.J.M., Garcia-Lazaro, J.A., McAlpine, D., and Schaette, R. (2020). Hidden hearing loss impacts the neural representation of speech in background noise. Curr. Biol. 30, 4710–4721.e4.

Moore, A.K., Weible, A.P., Balmer, T.S., Trussell, L.O., and Wehr, M. (2018). Rapid Rebalancing of Excitation and Inhibition by Cortical Circuitry. Neuron 97, 1341–1355.e6.

Natan, R.G., Briguglio, J.J., Mwilambwe-Tshilobo, L., Jones, S.I., Aizenberg, M., Goldberg, E.M., and Geffen, M.N. (2015). Complementary control of sensory adaptation by two types of cortical interneurons. eLife 4, 1–27.

Pachitariu, M., Stringer, C., and Harris, K.D. (2018). Robustness of spike deconvolution for neuronal calcium imaging. J. Neurosci. 38, 7976–7985.

Parthasarathy, A., Hancock, K.E., Bennett, K., DeGruttola, V., and Polley, D.B. (2020). Bottom-up and top-down neural signatures of disordered multi-talker speech perception in adults with normal hearing. eLife 9, e51419.

Petkov, C.I., O'Connor, K.N., and Sutter, M.L. (2007). Encoding of illusory continuity in primary auditory cortex. Neuron 54, 153–165.

Phillips, E.A.K., Schreiner, C.E., and Hasenstaub, A.R. (2017). Cortical interneurons differentially regulate the effects of acoustic context. Cell Rep. 20, 771–778.

Polley, D.B., Steinberg, E.E., and Merzenich, M.M. (2006). Perceptual learning directs auditory cortical map reorganization through top-down influences. J. Neurosci. 26, 4970–4982.

Qiu, C., Salvi, R., Ding, D., and Burkard, R. (2000). Inner hair cell loss leads to enhanced response amplitudes in auditory cortex of unanesthetized chinchillas: evidence for increased system gain. Hear. Res. 139, 153–171.

Rabinowitz, N.C., Willmore, B.D.B., King, A.J., and Schnupp, J.W.H. (2013). Constructing noise-invariant representations of sound in the auditory pathway. PLoS Biol. 11, e1001710.

Recanzone, G.H., Schreiner, C.E., and Merzenich, M.M. (1993). Plasticity in the frequency representation of primary auditory cortex following discrimination training in adult owl monkeys. J. Neurosci. *13*, 87–103.

Renart, A., de la Rocha, J., Bartho, P., Hollender, L., Parga, N., Reyes, A., and Harris, K.D. (2010). The asynchronous state in cortical circuits. Science *327*, 587–590.

Resnik, J., and Polley, D.B. (2017). Fast-spiking GABA circuit dynamics in the auditory cortex predict recovery of sensory processing following peripheral nerve damage. eLife *6*, e21452.

Robinson, B.L., Harper, N.S., and McAlpine, D. (2016). Meta-adaptation in the auditory midbrain under cortical influence. Nat. Commun. *7*, 13442.

Romero, S., Hight, A.E., Clayton, K.K., Resnik, J., Williamson, R.S., Hancock, K.E., and Polley, D.B. (2020). Cellular and widefield imaging of sound frequency organization in primary and higher order fields of the mouse auditory cortex. Cereb. Cortex *30*, 1603–1622.

Sametsky, E.A., Turner, J.G., Larsen, D., Ling, L., and Caspary, D.M. (2015). Enhanced GABAA-mediated tonic inhibition in auditory thalamus of rats with behavioral evidence of tinnitus. J. Neurosci. *35*, 9369–9380.

Sarro, E.C., von Trapp, G., Mowery, T.M., Kotak, V.C., and Sanes, D.H. (2015). Cortical Synaptic Inhibition Declines during Auditory Learning. J. Neurosci. *35*, 6318–6325.

Shaheen, L.A., Valero, M.D., and Liberman, M.C. (2015). Towards a Diagnosis of Cochlear Neuropathy with Envelope Following Responses. J. Assoc. Res. Otolaryngol. *16*, 727–745.

Takahashi, N., Oertner, T.G., Hegemann, P., and Larkum, M.E. (2016). Active cortical dendrites modulate perception. Science *354*, 1159–1165.

Takahashi, N., Ebner, C., Sigl-Glöckner, J., Moberg, S., Nierwetberg, S., and Larkum, M.E. (2020). Active dendritic currents gate descending cortical outputs in perception. Nat. Neurosci. *23*, 1277–1285.

Takesian, A.E., Kotak, V.C., and Sanes, D.H. (2012). Age-dependent effect of hearing loss on cortical inhibitory synapse function. J. Neurophysiol. *107*, 937–947.

Takesian, A.E., Bogart, L.J., Lichtman, J.W., and Hensch, T.K. (2018). Inhibitory circuit gating of auditory critical-period plasticity. Nat. Neurosci. *21*, 218–227.

Teichert, M., Liebmann, L., Hübner, C.A., and Bolz, J. (2017). Homeostatic plasticity and synaptic scaling in the adult mouse auditory cortex. Sci. Rep. *7*, 17423.

Turrigiano, G.G. (2008). The self-tuning neuron: synaptic scaling of excitatory synapses. Cell *135*, 422–435.

Vogels, T.P., Sprekeler, H., Zenke, F., Clopath, C., and Gerstner, W. (2011). Inhibitory plasticity balances excitation and inhibition in sensory pathways and memory networks. Science *334*, 1569–1573.

Whitton, J.P.P., Hancock, K.E.E., and Polley, D.B.B. (2014). Immersive audio-motor game play enhances neural and perceptual salience of weak signals in noise. Proc. Natl. Acad. Sci. USA *111*, E2606–E2615.

Whitton, J.P., Hancock, K.E., Shannon, J.M., and Polley, D.B. (2017). Audiomotor perceptual training enhances speech intelligibility in background noise. Curr. Biol. *27*, 3237–3247.e6.

Willmore, B.D.B., Cooke, J.E., and King, A.J. (2014). Hearing in noisy environments: noise invariance and contrast gain control. J. Physiol. *592*, 3371–3381.

Wu, P.Z., Liberman, L.D., Bennett, K., de Gruttola, V., O'Malley, J.T., and Liberman, M.C. (2019). Primary Neural Degeneration in the Human Cochlea: Evidence for Hidden Hearing Loss in the Aging Ear. Neuroscience *407*, 8–20.

Yang, S., Weiner, B.D., Zhang, L.S., Cho, S.-J., and Bao, S. (2011). Homeostatic plasticity drives tinnitus perception in an animal model. Proc. Natl. Acad. Sci. USA *108*, 14974–14979.

Yang, S., Su, W., and Bao, S. (2012). Long-term, but not transient, threshold shifts alter the morphology and increase the excitability of cortical pyramidal neurons. J. Neurophysiol. *108*, 1567–1574.

Yuan, Y., Shi, F., Yin, Y., Tong, M., Lang, H., Polley, D.B., Liberman, M.C., and Edge, A.S.B. (2014). Ouabain-induced cochlear nerve degeneration: synaptic loss and plasticity in a mouse model of auditory neuropathy. J. Assoc. Res. Otolaryngol. *15*, 31–43.

Zeng, F.G., Kong, Y.Y., Michalewski, H.J., and Starr, A. (2005). Perceptual consequences of disrupted auditory nerve activity. J. Neurophysiol. *93*, 3050–3063.

STAR★METHODS

KEY RESOURCES TABLE

REAGENT or RESOURCE	SOURCE	IDENTIFIER
Antibodies		
Mouse anti-CtBP2	BD Biosciences	612044; RRID:AB_399431
Mouse anti-GluA2	Millipore	MAB397
Rabbit anti-myosin-VIIa	Proteous Biosciences	25-670; RRID:AB_10015251
Goat anti-Mouse IgG2a Alexa Fluor 488	Invitrogen	A21131; RRID:AB_141618
Goat anti-Mouse IgG1 Alexa Fluor 647	Invitrogen	A21240; RRID:AB_141658
Goat anti-Rabbit IgG (H+L) Pacific Blue	Invitrogen	P10994
Bacterial and virus strains		
AAV5.Syn.GCaMP6s.WPRE.SV40	Chen et al., 2013	Addgene viral prep # 100843-AAV5
Chemicals, peptides, and recombinant proteins		
Lidocaine hydrochloride	Hospira Inc	Cat# 71-157-DK
Buprenorphine hydrochloride	Buprenex	Cat# NDC 12496-0757-5
Isoflourane	Piramal	Cat# NDC 66794-013-10
Silicon adhesive	WPI	Cat# KWIK-SIL
C&B Metabond Quick Adhesive Cement System	Parkell	Cat# S380
Ouabain octahydrate	Sigma-Aldrich	Cat# O3125
Deposited data		
Imaging and behavioral data	Mendeley Data	https://doi.org/10.17632/7n8tx3m5j9.1
Experimental models: organisms/strains		
Mouse: PVCre- B6;129P2-Pvalbtm1(cre)Arbr/J	The Jackson Laboratory	Stock No: 017320
Mouse:Ai14 - B6.Cg-Gt(ROSA)26Sortm14 (CAG-tdTomato)Hze/J	The Jackson Laboratory	Stock No: 007914
Software and algorithms		
Labview 2015	National Instruments	https://www.ni.com/en-us/shop/labview.html
ThorImage 3.0	Thorlabs	https://www.thorlabs.com/newgrouppage9.cfm?objectgroup_id=9072#ad-image-0
Suite2P	Github	https://github.com/cortex-lab/Suite2P
Registers2P	Github	https://github.com/cortex-lab/Suite2P/tree/master/registers2p
MATLAB 2016b	Mathworks	https://www.mathworks.com/products/matlab.html
Other		
Solenoid driver	Eaton-Peabody Lab	https://github.com/EPL-Engineering/epl_valve
Lickometer	Eaton-Peabody Lab	https://github.com/EPL-Engineering/epl_lickometer
PXI Controller	National Instruments	PXIe-8840
Ti-Sapphire laser	Spectra Physics	Mai Tai HP DeepSee
16x/.8NA Objective	Nikon	CFI75 LWD 16X W
Titanium headplate	iMaterialise	Custom
Two-Photon Microscope	Thorlabs	Bergamo II
Free-field speaker	Parts Express	275-010

RESOURCE AVAILABILITY

Lead contact

Further information and requests should be directed to and will be fulfilled by the lead contact, Daniel Polley (daniel_polley@meei.harvard.edu).

Materials availability
This study did not generate new unique reagents.

Data and code availability
Source data for the figures in the paper is available at Mendeley Data https://doi.org/10.17632/7n8tx3m5j9.1.

EXPERIMENTAL MODEL AND SUBJECT DETAILS

All procedures were approved by the Massachusetts Eye and Ear Animal Care and Use Committee and followed the guidelines established by the National Institutes of Health for the care and use of laboratory animals. PV-Cre × Ai14 mice of both sexes were used for this study. Mice were adult (8-9 weeks postnatal) at the time the first procedure for these experiments was performed. Mice were grouped housed unless they had undergone a survival surgery. Mice were maintained on a 12 hr light/12 h dark cycle with *ad libitum* access to food and water, unless undergoing behavioral testing. Mice undergoing behavioral testing were kept on a reversed 12hr light /12 hr dark cycle (7:00 a.m.-7:00 p.m). Mice were grouped-housed unless they had undergone a major survival surgery.

Data were collected from 29 mice. A total of twenty mice contributed data to the operant Go/NoGo behavior task (10 (5/5) during concurrent imaging and 10 without imaging (5/5, CND/Vehicle control). A total of nineteen mice contributed chronic two-photon imaging data in passive listening (N = 10/9, CND/Vehicle control).

METHOD DETAILS

Survival surgeries for awake, head-fixed experiments
Mice were anesthetized with isoflourane in oxygen (5% induction, 1.5%–2% maintenance). A homeothermic blanket system was used to maintain body temperature at 36.6° (FHC). Lidocaine hydrochloride was administered subcutaneously to numb the scalp. The dorsal surface of the scalp was retracted and the periosteum was removed. The skull surface was prepped with etchant (C&B metabond) and 70% ethanol before affixing a titanium head plate (iMaterialise) to the dorsal surface with dental cement (C&B metabond). At the conclusion of the headplate attachment and any additional procedures listed below, Buprenex (0.05 mg/kg) and meloxicam (0.1 mg/kg) were administered and the animal was transferred to a warmed recovery chamber.

Cochlear primary afferent neuropathy
Selective elimination of Type-I spiral ganglion neurons was achieved by applying a 1 mM solution of ouabain octahydrate (Sigma) and sterile water to the left and right round window niche, as described previously (Yuan et al., 2014). Animals were anesthetized with ketamine (120 mg/kg) and xylazine (12 mg/kg), with half the initial ketamine dose given as a booster when required. The connective tissue and underlying muscle were blunt dissected and held away from the bulla with retractors. A small opening was made in the bulla with the tip of a 28.5-gauge needle. The exposed round window niche was filled with 1–2 μL of ouabain solution using a blunted needle. Ouabain was reapplied five more times at 15 min intervals, wicking the remaining solution away with absorbent paper points before each application. For control experiments, sterile water was placed on the cochlear round window using an identical procedure. Measurements of the ABR and DPOAE (see below) were made periodically during ouabain application to confirm functionality and ABR threshold shift without changes in DPOAE thresholds or amplitudes. Additional ouabain was applied, as necessary, until the ABR threshold at 16 kHz had increased to a target range of 45-50 dB sound pressure level (SPL), which was a more moderate level of damage than used in our previous studies that targeted a near-complete elimination of cochlear afferent neurons. (Balaram et al., 2019; Chambers et al., 2016a, 2016b; Resnik and Polley, 2017).

Cochlear function tests
Mice were anesthetized with ketamine and xylazine (as above), and placed on a homeothermic heating blanket during testing. ABR stimuli were 5 ms tone pips at 8,12,16 or 32 kHz with a 0.5 ms rise-fall time delivered at 30 Hz. Intensity was incremented in 5 dB steps, from 20–80 dB SPL. ABR threshold was defined as the lowest stimulus level at which a repeatable waveform could be identified. DPOAEs were measured in the ear canal using primary tones with a frequency ratio of 1.2, with the level of the f2 primary set to be 10 dB less than f1 level, incremented together in 5 dB steps. The 2f1-f2 DPOAE amplitude and surrounding noise floor were extracted. DPOAE threshold was defined as the lowest of at least two continuous f2 levels, for which the DPOAE amplitude was at least two standard deviations greater than the noise floor. All treated animals underwent rounds of DPOAE and ABR testing three days before and two weeks after the nerve damage procedure. One mouse was excluded from the study because the ABR threshold shift at 16 kHz suggested minimal to no CND.

Cochlear histology
To visualize cochlear afferent synapses in one example neuropathic ear and one example control ear in a CND and vehicle control mice (Figure 1A), cochleae were dissected and perfused through the round window and oval window with 4% paraformaldehyde in phosphate-buffered saline, then post-fixed in the same solution for 1 hour. Cochleae were decalcified in 0.12M EDTA for 2 days and dissected into half-turns for whole-mount processing. Immunostaining began with a blocking buffer (PBS with 5% normal goat or

donkey serum and 0.2%–1% Triton X-100) for 1 hour at room temperature and followed by incubation with a combination of the following primary antibodies: 1) rabbit anti-CtBP2 at 1:100, 2) rabbit anti-myosin VIIa at 1:200, 3) mouse anti-GluR2 at 1:2,000. Lengths of cochlear whole mounts were measured and converted to cochlear frequency. Confocal z stacks from each ear at a matched mid-high frequency region were obtained in the inner hair cell area in a 1024 × 512 raster using a high-resolution glycerin-immersion objective (63x) and x3.17 digital zoom with a 0.25 μm z-spacing on a Leica SP5 confocal microscope. For each stack, the z-planes imaged included all synaptic elements in the x-y field of view.

Go / NoGo operant detection task

Three days after headplate surgery, animals were weighed and placed on a water restriction schedule (1 mL per day). During behavioral training, animals were weighed daily to ensure they remained above 80% of their initial weight and examined for signs of dehydration, such as fur tenting. Mice were given supplemental water if they received less than 1 mL during a training session or appeared excessively dehydrated. During testing, mice were head-fixed in a dimly lit, single-walled sound-attenuating booth, with their bodies resting in an electrically conductive cradle. Tongue contact on the lickspout closed an electrical circuit that was digitized (at 40 Hz) and encoded to calculate lick timing. Target tones and continuous broadband noise were independently delivered through a pair of co-localized inverted dome tweeters positioned 10 cm from the left ear. Digital and analog signals controlling sound delivery and water reward were controlled by a PXI system with custom software programmed in LabVIEW (National Instruments). Free-field stimuli were calibrated before recording using a wide-band ultrasonic acoustic sensor (Knowles Acoustics).

Most mice required 1-2 weeks of behavioral shaping before they could perform the complete tone detection task. After mice were habituated to head-fixation, they were conditioned to lick the spout within 2 s following the onset of a 12 kHz 70 dB SPL tone (0.5 s duration, with 5ms raised cosine onset-offset ramps), in order to receive a small quantity of water (4 μL). Target tones were presented either in quiet or during continuous 50 dB SPL white noise (0-50 kHz frequency range) with a variable inter-trial interval (4-10 s). Once reaction times were consistently < 1.2 s, additional levels were added (20-60, in 10 dB steps) and the tone duration was reduced to 50ms. During testing, tones were presented in blocks of quiet or white noise. Each block consisted of all tone intensities (20 to 70, in 10 dB steps) and catch trials where no tone was presented. False alarms triggered a 4-6 s time out. The order of the blocks and the levels within each block were randomized for each imaging session. In each session, each unique permutation of tone intensity and background noise condition was presented between 18-25 times, both in quiet and in noise. In some sessions, we also presented longer duration tones (0.5 s) in noise (Figure S1). Hits were defined as post-target licks that occurred > 0.15 s and < 1.2 s following the onset of the target tone. Entire sessions were excluded from analysis if the mouse was not under stimulus control, operationally defined as a false alarm rate in quiet (i.e., licking during the catch trials) > 20%, or hit rate for 70 dB tone presented in quiet < 80%. These exclusion criteria resulted in the elimination of < 4% of test sessions across all conditions (before, after, CND, or sham), underscoring that mice were reliably under stimulus control. Psychometric functions were fit using binary logistic regression. Threshold was defined as the point where the Go (lick) probability was equal or higher than 50%.

Virus mediated gene-delivery

For mice used in passive imaging experiments, two burr holes were made in the skull over the auditory cortex (1.75 - 2.25mm rostral to the lambdoid suture). A precision injection system (Nanoject III) was used to inject 75 nL of AAV5.Syn.GCaMP6s.WPRE.SV40 in each burr hole 190-230μm below the pial surface. For mice used in combined imaging and behavior experiments, the same virus injection procedure was performed during the cranial window surgery (see below).

Two-photon calcium imaging

Three round glass coverslips (one 4mm, two 3mm, #1 thickness) were etched with piranha solution and bonded into a vertical stack using transparent, UV-cured adhesive. Headplate attachment, anesthesia and analgesia follow the procedure described above. A 3 mm craniotomy was made over the right ACtx using a scalpel and the coverslip stack was cemented into the craniotomy. Animals recovered for at least 5 days before beginning water restriction for the tone detection task. An initial widefield epifluorescence imaging session was performed to visualize the tonotopic gradients of the ACtx and identify the position of A1 as described previously (Romero et al., 2020). Two-photon excitation was provided by a Ti:Sapphire-pulsed laser tuned to 940 nm. Imaging was performed with a 16 × /0.8NA water-immersion objective (Nikon) from a 512 × 512 pixel field of view at 30Hz with a Galvo-Resonant 8 kHz scanning microscope (Thorlabs). Scanning software was synchronized to the stimulus generation hardware using digital pulse trains. The microscope was rotated by 50-60 degrees off the vertical axis to obtain images from the lateral aspect of the mouse cortex while the animal was maintained in an upright head position. Imaging was performed in a light-tight, sound attenuating chamber mounted on a floating table. Animals were monitored throughout the experiment to confirm all imaging was performed in the awake condition using modified cameras coupled to infrared light sources. Imaging was performed in layers L2/3, 175-225 μm below the pial surface. Fluorescence images were captured at 2x digital zoom, providing an imaging field of (0.42 × 0.42 mm). Raw calcium movies were processed using Suite2P, a publicly available two-photon calcium imaging analysis pipeline (Pachitariu et al., 2018). Briefly, movies are registered to account for brain motion. Regions of interest are established by clustering neighboring pixels with similar time courses. Manual curation is then performed to eliminate low-quality or non-somatic regions of interest. Spike deconvolution was also performed in Suite2P, using the default method based on the OASIS algorithm (Friedrich et al., 2017). For Figure S3, ΔF/F was computed as (F(t) – F0)/F0, where F(t) was the raw calcium signal and F0 was the mean baseline fluorescence prior to stimulus presentation

Neuron
Article

CellPress

across trials. Cross-day image registration was done with the registers2p function in Suite 2P, using both the red (tdTomato) and green (GCaMP) channels. This approach allowed us to follow the same cells throughout the experiments. On average, each field of view produced 181.6 ± 6.17 (mean ± SEM) PPy and 16.99 ± 0.45 PV neurons, of which an average of 106.9 ± 1.96 PPy and 7.68 ± 0.33 PV neurons were tracked throughout the imaging period.

During each passive imaging session, 12 kHz tones (as described above) were presented at 20-80 dB SPL (in 10 dB steps) in two blocks. One block presented the tones in quiet and the second block presented the tones during continuous broadband noise (as described above). Each block consisted of 25 repetitions of all intensities. Block order and intensity sequencing was randomized for each imaging session. During concurrent imaging and behavior, tones and water rewards were presented as described above.

QUANTIFICATION AND STATISTICAL ANALYSIS

Two-photon imaging analysis

All analysis was performed on the deconvolved calcium activity traces unless otherwise stated. During passive imaging experiments, spontaneous activity during silence or continuous noise were calculated from the 825 ms preceding tone onset. The PPy-PV symmetry index for Figure 2G was calculated by first obtaining the mean activity rates of all PPy and PV cells within the imaging field separately, and then calculating the asymmetry index as (PPy - PV) / (PPy + PV). Sound-evoked activity rates for sound in quiet or in noise, were calculated as the z-score relative to the spontaneous activity of each cell per trial. When analyzing the fractional change in GCaMP fluorescence, tone evoked activity was calculated as the difference between the average activity in the post stimulus window (100ms straddling the peak activity frame in the 500ms following the tone presentation) to pre-stimulus window (100ms straddling the peak activity frame in the 500ms preceding the tone presentation). Gain was defined as the relationship between sound level (input) and activity rate (output). The gain was calculated as the average change in activity between 10 dB steps in the rising phase of the rate-level function.

To quantify correlated activity between cells during behavioral detection of tones in noise, we cross-correlated the z-scored activity of neuron pairs during the 2.7 s period prior to the tone presentation. The degree of correlated activity between each pair was defined as the size of the positive area under the peak of the cross-correlogram closest to zero lag time point (xcorr area). The peak was defined as a positive data point larger or equal to its neighboring data points that was preceded or followed by another positive data point. If such a peak wasn't found in the correlogram of a specific pair, or if it was located at the borders of the measurement window, the cross correlation between that pair was excluded from further analyses.

To determine how ensemble activity decoded tone presence or behavioral outcomes (hit versus miss), we used a support vector machine classifier (SVM) with a linear kernel. We fit the classifier model to a data matrix of cell activity. For tone classification in passive experiments (Figure 4), the data matrix consisted of the mean activity rate within 100ms period just before or after stimulus onset. For the classification of miss versus hit behavioral outcome, the data matrix consisted of the mean activity rate within 100 ms following the tone presentation before licking occurred (Figure 5) or the degree of synchrony before the tone presentation (xcorr area – see above, Figure 6). Ensemble analyses included all identified neurons in any given field of view. To reduce the influence of any possible inequities in sample sizes across mice or conditions, and to avoid overestimation and an unstable result resulting from the larger number of features than the number of samples, we used principal components analysis to reduce dimensionality of the data matrix before classification. We ran the SVM on the principal components that explained 90% of the variance to classify stimulus presence or behavioral outcome. Leave one-out cross-validation was then used to train the classifier and compute a misclassification rate on the untrained trial. This process was then iterated according to the number of trials in a given imaging session. We repeated this process for each mouse and for each imaging session independently and calculated the mean decoding accuracy across sessions. As a control (Figure S4), we repeated this analysis on mean pre- stimulus activity, on the degree of synchronized activity between pairs of cells' reshuffled activity traces and on the degree of synchronized activity between the activity of pairs of cells taken from different trials, and tested whether they could predict the behavioral outcome. The SVM training and cross-validation procedure was carried out in MATLAB using the 'fitcsvm', 'crossval', and 'kfoldLoss' functions.

Statistical analysis

All statistical analyses were performed in MATLAB 2016b (Mathworks). Data are reported as mean ± SEM unless otherwise indicated. Post hoc pairwise comparisons were corrected for multiple comparisons using the Bonferroni correction. Greenhouse-Geisser correction was used when assumption of sphericity was violated.